JOURNAL OF MATERIALS SCIENCE 19 (1984) 801–808

Young's modulus of porous materials

Part 1 *Theoretical derivation of modulus–porosity correlation*

JAMES C. WANG*
State University of New York, Stony Brook, New York 11794, USA

A relationship between porosity and Young's modulus is obtained theoretically for porous materials made by powder metallurgy. The relationship is applicable to the entire range of porosity and is capable of treating the transition of pore structure from interconnected to isolated. The exact solution is presented graphically. An approximate solution with a wide applicable porosity range is given.

1. Introduction

From the literature [1, 2] it has long been accepted that for porous materials both the strength, S, and the Young's modulus, E, can be described empirically by

$$S = S_0 \exp(-ap) \quad (1)$$

$$E = E_0 \exp(-bp) \quad (2)$$

respectively, where S_0 is the zero-porosity strength, E_0 is the zero-porosity Young's modulus, p is the porosity, and a and b are material constants. These two equations are known as the Ryshkewitch–Duckworth equation and the Spriggs' equation, respectively, and yield straight lines when plotted in semilogarithmic form (Fig. 1). They are entirely empirical, not based on theory.

Various theories have been developed for materials consisting of a continuous matrix and a dispersed second phase of specific shape and orientation [3–6]. These theories were subsequently applied to porous materials by considering the second phase to be vacuum. Since the existing theories are based on isolated dispersoids or holes, they do not apply to porous materials with interconnected pores, a situation which is typical for the early and intermediate stages of powder consolidation (such as hot pressing, HIPing (hot isostatic pressing) and sintering). The only analytical work of fundamental importance was carried out on strength by Knudsen [7]. In his work he obtained a strength–porosity relation analytically and then compared it with the Ryshkewitch–Duckworth empirical equation. To the author's knowledge, no parallel work on Young's modulus has been published.

In this paper an analysis is carried out on the Young's modulus of porous materials fabricated by the methods of powder metallurgy. The theoretical results will be compared with the empirical Spriggs' equation.

2. Physical model

2.1. Knudsen's model

Prior to choosing an appropriate model, it is necessary to mention Knudsen's work [7] on strength which will be discussed. Knudsen made the following assumptions: (a) the pores are formed by packing equal-sized spheres in a special array, such as simple cubic stacking, etc.; (b) various porosities can be achieved by densifying to different densities; (c) the spheres are attracted to one another during densification, causing the contact area to increase, yet without disturbing the relative orientation of the spheres, so that the pattern of the array remains unchanged; (d) each deforming sphere maintains its original volume, and the displaced material redistributes itself evenly over the residual spherical surfaces; (e) the strength of an individual sphere is stronger than the cohesion of the contacting area, the latter being the weakest link of the material; (f) the strength of a porous material is proportional to the load-bearing contact area.

*Present address: SCM Corporation Research Laboratory, 11000 Cedar Avenue, Cleveland, Ohio 44106, USA.

0022–2461/84 $03.00 + .12

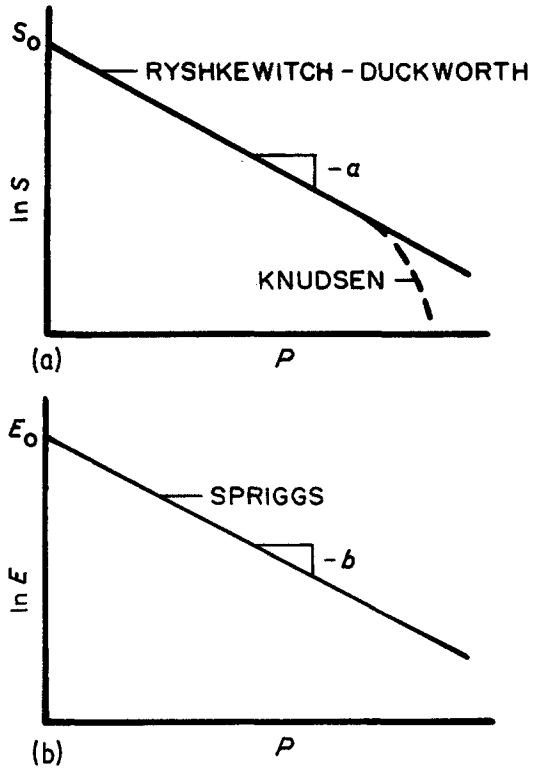

Figure 1 Empirical equations for strength and Young's modulus as functions of porosity. (a) Ryshkewitch–Duckworth equation for strength. (b) Spriggs' equation for Young's modulus.

Using a point-by-point calculation of the contact area as a function of bulk density, Knudsen was able to obtain a straight-line semilogarithmic relationship, as predicted by Equation 1, between strength and porosity for a reasonably wide range of porosity.

2.2. Physical model for Young's modulus

In the present Young's modulus study, a model similar to Knudsen's will be used, the first four assumptions given above being adopted. The initial density is defined here as the packing density at which the spheres just touch. For simplicity, simple cubic stacking pattern is chosen.

As depicted in Fig. 2a, for a simple cubic array, the "lattice parameter" is l, each lattice cell containing one "lattice point". The spatial territory of a lattice point is a cube centred at the lattice site, a cube side being l. The sequence of events associated with a unit cell during densification is given in Fig. 2d. Upon densification the neighbouring spheres will coalesce to form flattened areas. Each flattened area sustains an angle about the centre of the sphere, half of the angle being defined as θ, the angle of coalescence.

At a given instant, the powder particle occupies a volume confined to a sphere of radius R and truncated by the unit cell of lattice parameter l. At the very beginning of densification the sphere is inscribed within the unit cell, with $\theta = 0$. As densification proceeds, l decreases with increasing R and θ. The sphere deforms to a "spherical polyhedron", partly sphere and partly polyhedron, where R is the radius of the spherical portion. When θ reaches 45° the pores become disconnected. Upon further densification, the flattened area is no longer a full circle, and the residual spherical surfaces retreat towards the cell corners. Finally, at 100% density, the residual spherical surfaces shrink into points which coincide with the cell corners, and the corresponding θ is the angle between the directions [1 0 0] and [1 1 1], or $\theta = 54.74°$.

This model is inherently capable of treating the transition of the pore structure from interconnected to disconnected.

3. Mathematical analysis

3.1. Basic derivations

Due to periodicity, the consideration of the behaviour of a unit cell is equivalent to the consideration of the entire porous body.

At any stage of densification, hence any given θ, the cell volume is

$$V_0 = l^3$$

and the volume of the powder is

$$V = \int_{-l/2}^{l/2} A \, dz$$

where A is the cross-sectional area of the powder perpendicular to the z-axis. The volume fraction, and hence the relative density, is

$$X \equiv \frac{V}{V_0} = \frac{1}{l^3} \int_{-l/2}^{l/2} A \, dz. \qquad (3)$$

When the unit cell is subject to a load P in the z-direction, as shown in Fig. 2b, the elongation is

$$\delta = \int_{-l/2}^{l/2} \frac{P/A}{E_0} dz$$

and the apparent Young's modulus is

$$E \equiv \frac{P/l^2}{\delta/l}$$

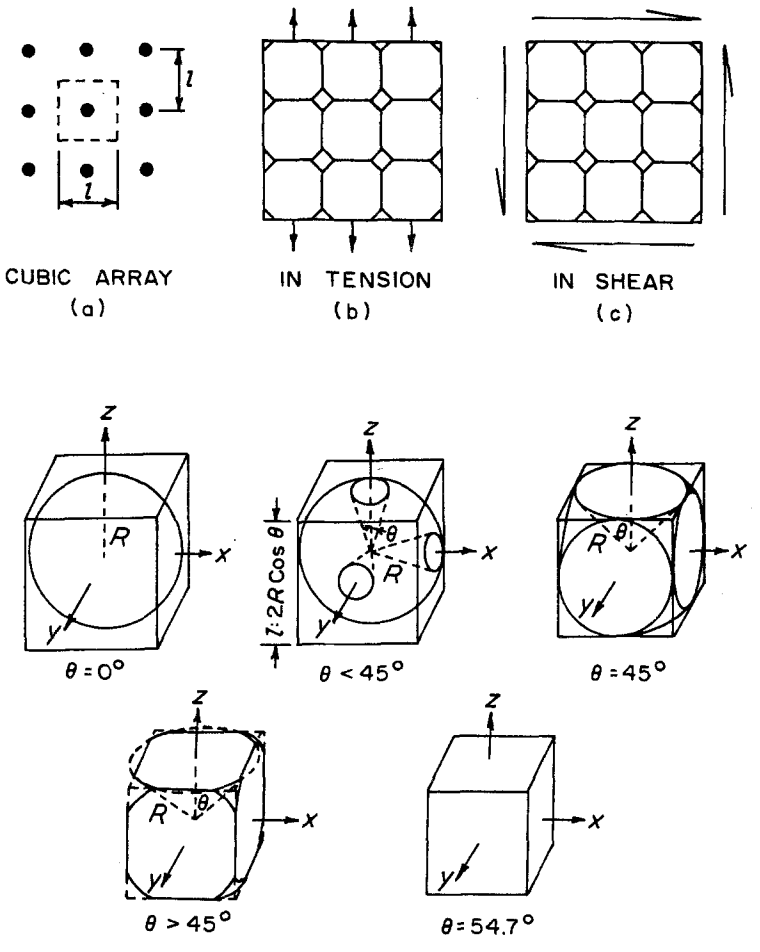

Figure 2 Simple cubic array and unit cell.

or

$$\frac{E}{E_0} = \left(l \int_{-l/2}^{l/2} \frac{dz}{A} \right)^{-1} \tag{4}$$

Equations 3 and 4 appear to be functions of l, but upon mathematical manipulation [8], X and E/E_0 become functions of θ only; see the Appendix. $X(\theta)$ and $E/E_0(\theta)$ are complicated functions of θ, which require numerical integration to evaluate. The results are tabulated in Table I and plotted as Curve 1 in Fig. 3.

If P is applied in a shear mode as shown in Fig. 2c and δ is the corresponding shear displacement, then the same foregoing derivations are equally applicable to the shear modulus, and the porosity dependency of shear modulus is identical to that of Young's modulus. Therefore, Curve 1 also represents the shear modulus–density relationship

$$\frac{G}{G_0} = \frac{E}{E_0}. \tag{5}$$

3.2. Shear contribution and bending contribution

The above derivations and the resulting Curve 1 are for the ideal case where P is exerted on a perfect simple-cubic array in the z-direction. In reality, nonideal cases prevail, as shown in Fig. 4b. The particles do not always achieve perfect stacking and the [1 0 0] direction is not always parallel to the load. The result is that the neighbouring particles are out of alignment with the load, as illustrated in Fig. 4c. As can be seen from Fig. 4b, nonideal alignment does not significantly affect the density but, as will be seen later, it does affect the Young's modulus result. Therefore, corrections to the ideal case and Curve 1 will be made accordingly.

TABLE I Numerical values for theoretical curves

X	p	E/E_0	E_1^{eff}/E_0	E_2^{eff}/E_0
0.5236	0.4764	0	0	0
0.5246	0.4754	0.1943	0.07506	0.02899
0.5274	0.4726	0.2347	0.09151	0.03568
0.5354	0.4646	0.2832	0.11334	0.04536
0.5476	0.4524	0.3273	0.13615	0.05664
0.5612	0.4388	0.3635	0.15761	0.06833
0.5780	0.4220	0.4006	0.18235	0.08301
0.5979	0.4021	0.4390	0.21114	0.10154
0.6209	0.3791	0.4795	0.24484	0.12502
0.6471	0.3529	0.5224	0.28443	0.15485
0.6764	0.3236	0.5680	0.33074	0.19257
0.7088	0.2912	0.6165	0.38473	0.24010
0.7439	0.2561	0.6676	0.44691	0.29916
0.7815	0.2185	0.7211	0.51768	0.37166
0.8208	0.1792	0.7759	0.59640	0.45843
0.8610	0.1390	0.8304	0.68143	0.55915
0.9002	0.0998	0.8823	0.76859	0.66956
0.9362	0.0638	0.9278	0.85135	0.78123
0.9651	0.0349	0.9622	0.91884	0.87745
1.00	0	1	1	1

Let us first consider the lines of force. It is well known that the lines of force can pass across grain boundaries, but not through holes. At zero porosity, both the ideal and the nonideal cases reach the same morphology, i.e. solidly packed with no pores to disturb the force-line flux. This is illustrated in Figs. 5a and b, where M is the misalignment. The lines of force are straight and symmetrical about the z-axis. Therefore, the Young's modulus is equal to E_0 for both the ideal and the nonideal cases. However, at nonzero porosites, Fig. 5c, the lines of force are bent and are asymmetrical about the z-axis, which converts the applied load into a combination of tension and shear. The total elongation, Fig. 4d, is the sum of tensile elongation, δ_E, and shear displacement, δ_G. As a result, the effective Young's modulus includes a shear modulus component. To include the shear contribution in the effective Young's modulus, let us write

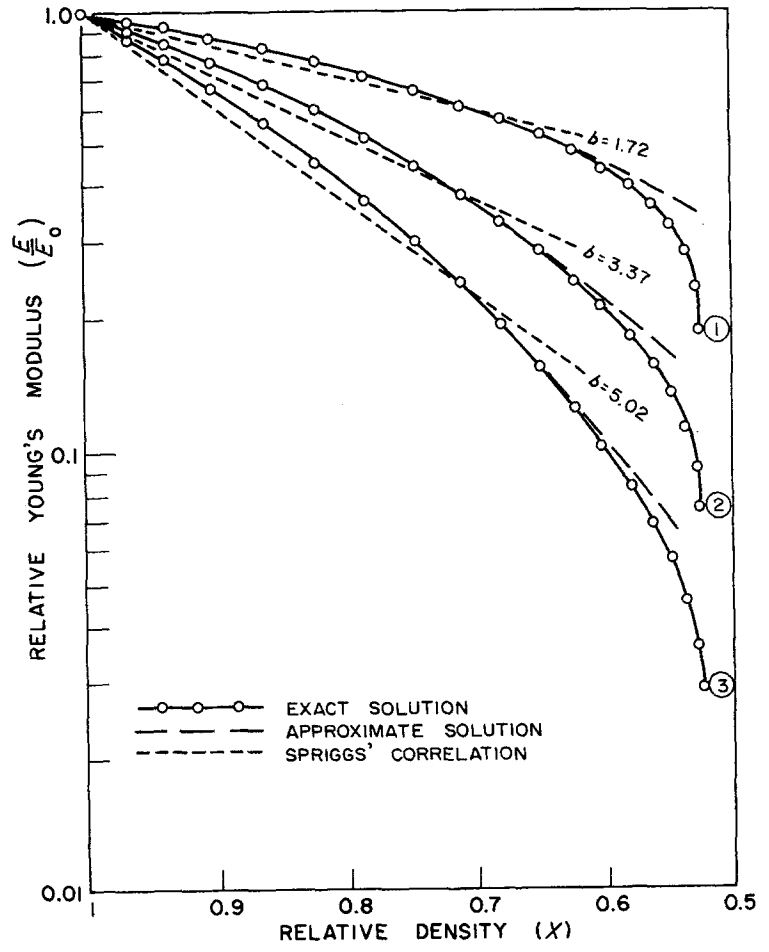

Figure 3 Young's modulus of porous materials. Solid curves are the theoretical curves, broken curves are the approximate solutions and the dotted lines are the Spriggs' correlation lines.

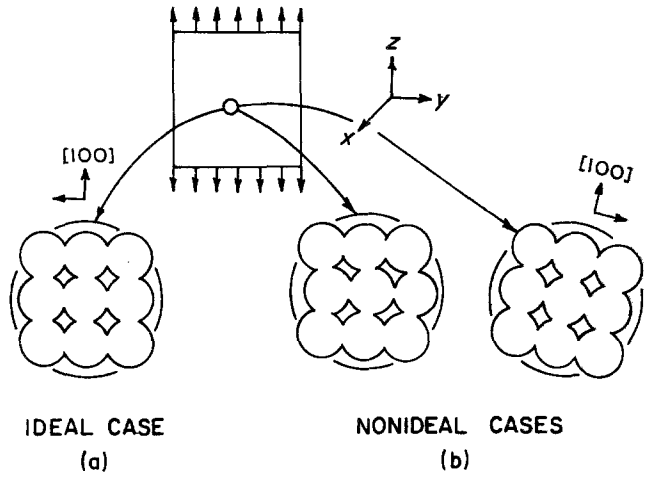

Figure 4 Effects of nonideal alignment on the elongation in the z-direction.

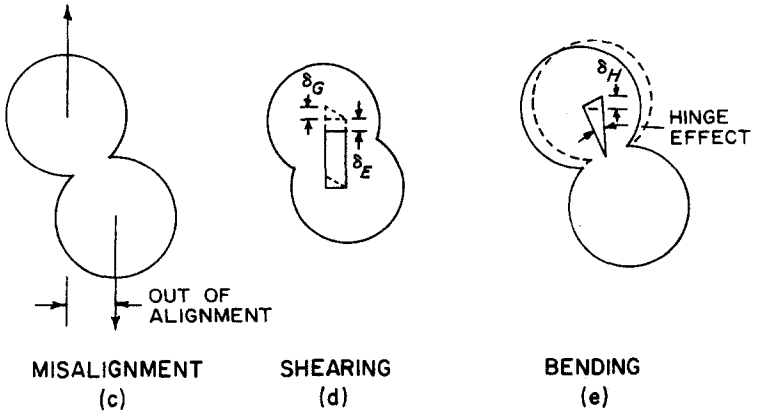

$$E_1^{\text{eff}} = \bar{W}_E E + \bar{W}_G G \tag{6}$$

where $\bar{W}_E$ and $\bar{W}_G$ are the weight fractions.

Substituting Equation 5 in Equation 6 and normalizing with respect to E_0,

$$\frac{E_1^{\text{eff}}}{E_0} = \left(\bar{W}_E + \frac{G_0}{E_0}\bar{W}_G\right)\frac{E}{E_0} \tag{7}$$

where $[\bar{W}_E + (G_0/E_0)\bar{W}_G]$ is the correction factor for the shear effect.

It is necessary to determine $\bar{W}_E$ and $\bar{W}_G$ as functions of porosity. Since we know that progressively the E component gains importance and the G component loses importance as the porosity decreases, therefore a lever-rule weight fraction relation is proposed:

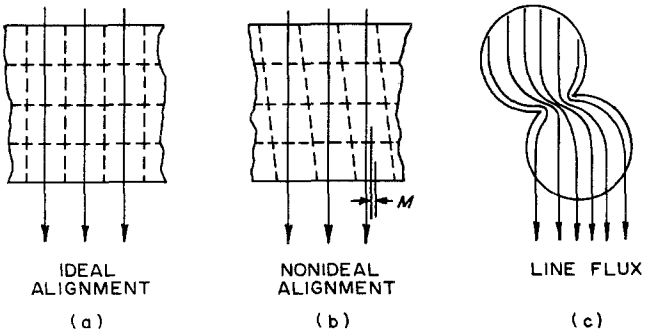

Figure 5 The lines of force.

$$W_E = \frac{p_i - p}{p_i}$$

and

$$W_G = \frac{p}{p_i}$$

where p_i is the initial packing porosity and p is the instantaneous porosity. This lever-rule type of relation is proposed for the beauty of simplicity and because it satisfies the boundary conditions, i.e. $E_1^{eff} = E_0$ at $p = 0$ and $E_1^{eff} = 0$ at $p = p_i$.

By using lever-rule weight fractions, Equation 7 can now be written as

$$\frac{E_1^{eff}}{E_0} = \left[\frac{p_i - p}{p_i} + \frac{G_0}{E_0}\frac{p}{p_i}\right]\frac{E}{E_0}(\theta) \qquad (8)$$

The ratio of G_0 to E_0, which can be obtained experimentally, depends slightly on material, and depends on the Poisson's ratio. For example, for alumina, G_0/E_0 has been measured to be in the range of 0.38 to 0.40 [9–13]. For the present work a value of 0.385 is chosen because this value corresponds to a Poisson's ratio of 0.3, which is an appropriate value between ductile metals and brittle refractories. The initial packing density, p_i, is 0.4764 for a simple cubic array. Substituting 0.4764 for p_i and 0.385 for G_0/E_0 into Equation 8, the resulting E_1^{eff}/E_0 is tabulated in Table I and plotted as Curve 2 in Fig. 3.

In addition to the shear effect, the non-ideal alignment also forces the neck to act as a stiff hinge in order to improve alignment. This situation is illustrated in Fig. 4e. A correction factor for this hinge effect is necessary. Since the hinge becomes stiffer with increasing neck size, the porosity dependency of the hinge effect follows the same trend as does shear deformation. Therefore, to a first approximation, the correction factor for shear is likewise used to correct the hinge effect. After correcting the hinge effect on E_1^{eff}, the new effective Young's modulus E_2^{eff} becomes

$$\frac{E_2^{eff}}{E_0} = \left[\frac{p_i - p}{p_i} + \frac{G_0}{E_0}\frac{p}{p_i}\right]^2\frac{E}{E_0}(\theta). \qquad (9)$$

The results are given in Table I and shown as Curve 3 in Fig. 3.

Like E, the effective E_1^{eff} and E_2^{eff} are functions of θ alone, not functions of l or R. This means that the Young's modulus is determined by the degree of densification, hence the porosity, but not by the size of the powder particles which make up the porous body.

4. Discussions

4.1. Approximate solution

The theoretical curves are the exact solutions. These curves lend support to Spriggs' correlation for narrow porosity ranges, particularly at high densities. However, for correlating data over a wider range of porosity, the b-value in Equation 2 cannot be treated as constant, and the exponent in Equation 2 cannot be considered a linear function of porosity. This is especially evident at high porosities.

In fact, the theoretical curves already deviate from linearity at the very beginning of the curves, i.e. $p = 0$ with negative second derivatives. In view of the negative second derivative, an approximated solution with a quadratic exponent is proposed:

$$E = E_0 \exp\left[-(bp + cp^2)\right] \qquad (10)$$

which is quite satisfactory over a wide porosity range. For example, the theoretical curves 1, 2 and 3 can be approximated by Equation 10 with (b, c) equal to (0.946, 2.54), (2.15, 4.01) and (3.35, 5.48), respectively, as shown by the broken curves in Fig. 3. The accuracy is well within ± 2% throughout the porosity range from $p = 0$ to $p = 0.38$. For comparison, the corresponding Spriggs' correlations, covering the same porosity range ($p = 0$ to $p = 0.38$), are given by the straight lines in Fig. 3, with b equal to 1.72, 3.37 and 5.02, respectively. It is obvious that the present analysis is a much-improved correlation over Spriggs' equation. Additional high-order terms can be included for the region where the density is very close to the packing density:

$$E = E_0 \exp\left[-(bp + cp^2 + dp^3 + \ldots)\right]. \qquad (11)$$

All the coefficients are non-negative, as dictated by the shape of the theoretical curves.

4.2. Effect of neck geometry

Up to this point the neck resulting from particle–particle contact has been assumed to be Type A–A, as depicted in Fig. 6. In reality, surface processes (e.g. surface diffusion, surface-tention-induced local plastic flow) may take place during densification. Therefore, a more realistic model would be model B–B. At any given density the contact area of type B–B is greater than that of A–A. This effect is likely to be significant only at the initial stage of densification and will decrease progressively with increasing density.

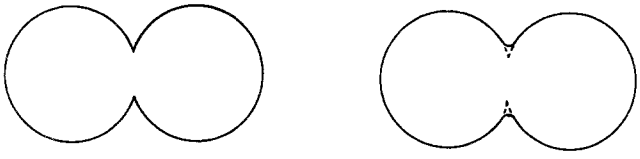

Figure 6 Neck groove geometries.

For the case of model B–B, the enlargement of the contact area will only locally reduce the elongation, δ, in the vicinity of the neck and will not affect the δ's farther away from the contact area. The effect is only partially reflected in E. Consequently, no significant difference is expected in E-values between models A–A and B–B.

4.3. Particle size and grain growth

The foregoing analysis is based on a model for which the specimens are comprised of equal-sized powder particles, each particle retaining its initial volume during densification. Consequently a test can be applied only to specimens of similar particle size and with no grain growth. Fortunately, the analysis indicates that the Young's modulus is governed by the degree of densification, θ, (hence, governed by density) and is independent of particle size, R. Therefore, the present results can be used to correlate data generated from specimens having different particle size or where grain growth occurs during densification, provided that within each specimen there is only one particle size. Of course, all the specimens must be of the same material and have the same stacking pattern.

4.4. Non-simple cubic systems

Since simple cubic stacking dictates a packing density of 0.524, strictly speaking, similar analyses should be conducted on bcc, fcc and other arbitrary arrays, where the initial packing density is different from 0.524. However, Equation 10 (or Equation 11) should be applied to nonsimple cubic arrays, as well. Since Equation 2 does not hold true for simple cubic systems, there is no logical reason to expect that it will hold true for other systems. Further, if Equation 2 indeed prevails in other systems, curve fitting will result in zero or negligibly small values for all the coefficients except b, which automatically reduces Equation 10 or Equation 11 to Equation 2.

5. Conclusion

The effect of porosity on Young's modulus has been obtained and presented in Fig. 3. The theoretical relation can be approximated by

$$E = E_0 \exp\left[-(bp + cp^2)\right].$$

Higher-order terms can be added to the exponent for the region where the density is very close to the packing density. All of the coefficients (b, c, etc.) are nonnegative numbers, as dictated by the shape of the theoretical curves.

The present analysis is inherently capable of treating the transition of the pore structure from interconnected to isolated.

Appendix

By introducing a new variable ϕ as defined by Fig. A1, one obtains:

$$X(\theta) = \begin{cases} \dfrac{\pi}{12}\left(\dfrac{9}{\cos^2\theta} - 3 - \dfrac{4}{\cos^3\theta}\right) & \text{for } \theta \leqslant 45^\circ \\ (\tan^2\theta - 1)^{1/2} + \dfrac{1}{4\cos^3\theta} \displaystyle\int_\theta^{\sin^{-1}[(2)^{1/2}\cos\theta]} [\sin^3\phi(\pi - 4\alpha + 2\sin 2\alpha)]\, d\phi & \text{for } \theta \geqslant 45^\circ \end{cases}$$

$$\frac{E}{E_0}(\theta) = \begin{cases} \dfrac{1}{4\cos\theta}\left[\dfrac{1}{\pi}\ln\dfrac{\tan(\pi/4 - \theta/2)}{\tan(\theta/2)} + \displaystyle\int_{\pi/2-\theta}^{\pi/2} \frac{d\phi}{\sin\phi(\pi - 4\alpha + 2\sin 2\alpha)}\right]^{-1} & \text{for } \theta \leqslant 45^\circ \\ \left[(\tan^2\theta - 1)^{1/2} + 4\cos\theta \displaystyle\int_\theta^{\sin^{-1}[(2)^{1/2}\cos\theta]} \frac{d\phi}{\sin\phi(\pi - 4\alpha + 2\sin 2\alpha)}\right]^{-1} & \text{for } \theta \geqslant 45^\circ \end{cases}$$

where $\alpha \equiv \cos^{-1}(\cos\theta/\sin\phi)$.

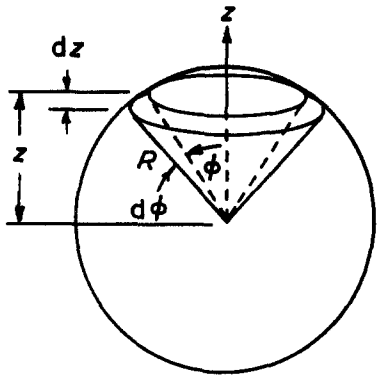

Figure A1 The relation between variables ϕ and z.

References

1. W. H. DUCKWORTH, *J. Am. Ceram. Soc.* **36** (1953) 68.
2. R. SPRIGGS, *J. Am. Ceram. Soc.* **44** (1961) 628.
3. F. GATTO, *Alluminio* **19** (1950) 19.
4. J. K. MACKENZIE, *Proc. Phys. Soc. (London)* **63B** (1950) 2.
5. B. D. AGARWAL, G. A. PANIZZA and L. J. BROUTMAN, *J. Am. Ceram. Soc.* **54** (1971) 620.
6. Z. HASHIN, *J. Appl. Mech.* **29** (1962) 143.
7. F. KNUDSEN, *J. Am. Ceram. Soc.* **42** (1959) 376.
8. J. C. WANG, Ph.D. Thesis, State Univ. of New York at Stony Brook, NY, USA (1978).
9. E. RYSHKEWITCH, *J. Am. Ceram. Soc.* **34** (1951) 322.
10. A. NAGARAJAN, *J. Appl. Phys.* **42** (1971) 3693.
11. E. SCHREIBER, *J. Am. Ceram. Soc.* **51** (1968) 541.
12. D. H. CHUNG, W. B. CRANDALL and W. G. LAWRENCE, *Bull. Ceram. Res.*, No. 297, College of Ceram., Alfred Univ. (1961) unpublished.
13. O. L. ANDERSON and N. SOGA, "Sum. Tech. Rept., AF-AFOSR Contract No. AF 33 (615-1700)", Lamont Geological Observatory, Columbia Univ. (1965) unpublished.

Received 14 June
and accepted 28 June 1983